

Cracking elements method with a dissipation-based arc-length approach

Yiming Zhang^{a,*}, Junguang Huang^a, Yong Yuan^{b,c}, Herbert A. Mang^{d,**}

^a School of Civil and Transportation Engineering, Hebei University of Technology, Xiping Road 5340, 300401, Tianjin, PR China

^b Department of Geotechnical Engineering, Tongji University, Siping Road 1239, 200092, Shanghai, PR China

^c State Key Laboratory for Disaster Reduction in Civil Engineering, Tongji University, Siping Road 1239, 200092, Shanghai, PR China

^d Institute for Mechanics of Materials and Structures (IMWS), Vienna University of Technology, Karlsplatz 13/202, 1040, Vienna, Austria

ARTICLE INFO

Keywords:

Cracking elements method
Quasi-brittle fracture
Path following
Arc-length method
Energy dissipation

ABSTRACT

The dissipated strain energy, representing a monotonically increasing state variable in nonlinear fracture mechanics, can be used to develop an arc-length constraint equation for tracking the energy dissipation path instead of the elastic unloading path of the response of a structure. This was the motivation for the development of a dissipation-based arc-length method, followed by its implementation in the framework of the recently proposed Global Cracking Elements Method (GCEM). The dissipated energy is extracted with the help of the crack openings and tractions, i.e. by means of the displacement jumps and the cohesive forces between the two surfaces of a crack. The stiffness factor of the arc-length constraint equation is obtained in the solution process by means of the Sherman-Morrison formula. Several numerical tests are performed. The results demonstrate the robustness of the proposed method. It captures both global and local peak loads and all snap-back parts of the force-displacement responses of loaded structures with multiple cracks.

1. Introduction

Loading of structures made of quasi-brittle material results in a strong and almost instant stress release and redistribution in consequence of the strain softening process [1], starting when a local or the global peak load is reached. Usually this process results in numerical instability, characterized by snap-through and snap-back behavior at force or displacement control [2]. Path-following methods, among which the arc-length method is the most successful one, allow tracking the equilibrium path in a continuous and robust manner.

Arc-length methods commonly introduce a new unknown load control, which is treated together with the original balance equation. Correspondingly, a new constraint equation is formed to obtain a monotonically increasing state variable during the loading process. Therefore, the loading path can be followed smoothly, and failure of the analysis when tracking the elastic unloading path can be avoided. The increment of the state variable correlates with the prescribed arc length. Conventionally, the state variable is associated with the displacements. When considering the global displacements, for example, by adopting the sum of the incremental displacements as the state variable, its monotonic increase cannot be assured. It was shown that consideration of the local dis-

placements, i.e., of the crack mouth displacements (opening or sliding), generally provides more stable results [3]. Unfortunately, in engineering practice, the positions of the crack mouths are usually not known a priori. Therefore, a more reliable state variable for automatically tracking the dissipation path is advantageous.

For structures experiencing cracking, damage and dissipation of strain energy are irreversible processes. Hence, the dissipated energy is an ideal state variable for the arc-length method. By definition, the dissipated energy is the energy released when cracks initiate, propagate, even get wider. For cohesive cracks, the dissipated energy is the total work done by the cohesive forces across the cracks. In early works [4,5], the internal energy and the work done by the external loads are used to obtain the dissipated energy. Later, the authors of [2] have shown that the same procedure can be applied, with both the internal and the dissipated energy following the entire loading path, where the switch of the arc-length state variable can be controlled by a scale factor. Energy-based arc-length methods were successfully applied in Refs. [6–9]. Moreover, a hybrid version was recently proposed in Ref. [10] as a combined displacement- and dissipation-based arc-length method to enhance the numerical stability.

The Cracking Elements Method (CEM) is a novel numerical

* Corresponding author.

** Corresponding author.

E-mail addresses: yiming.zhang@hebut.edu.cn (Y. Zhang), herbert.mang@tuwien.ac.at (H.A. Mang).

<https://doi.org/10.1016/j.finel.2021.103573>

Received 27 January 2021; Received in revised form 21 March 2021; Accepted 22 March 2021

Available online XXX

0168-874X/© 2021 Elsevier B.V. All rights reserved.

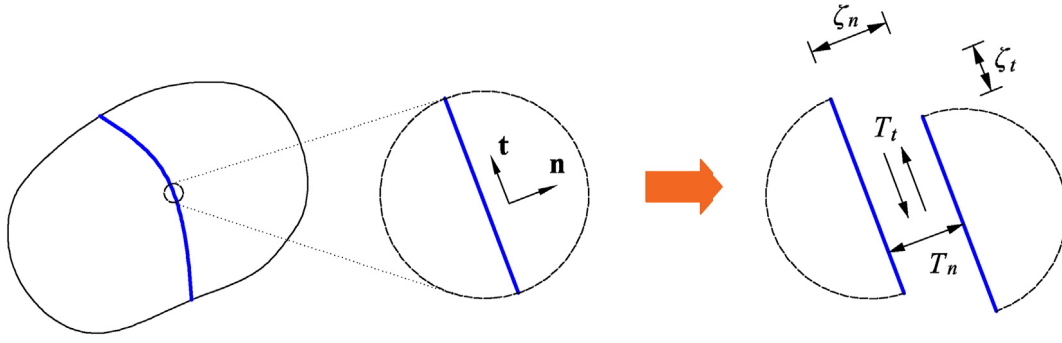


Fig. 1. Definitions of \mathbf{n} , \mathbf{t} , $[\zeta_n, \zeta_t]$ and $[T_n, T_t]$

approach for simulating quasi-brittle fracture [11,12]. It was inspired by the cracking particle method [13–15] which also uses piece-wise disconnected cracking segments to represent regions of cracking. This avoids precise descriptions of crack tips and continuities of crack paths, greatly simplifying the crack tracking strategy [16]. Only element-wise crack orientation is needed. The CEM is a crack-opening based approach that uses the characteristic length like some of the damage-degree based models [17,18]. In a global/enriched treatment [19], the crack openings of the CEM can be introduced as global degrees of freedom, making it possible to extract the dissipated energy.

In this work, a dissipation-based arc-length approach for the CEM is proposed and implemented into the CEM framework. The features of this work are as follows:

- The dissipated energy is directly determined by the crack openings and tractions as opposed to indirect determination by forces and displacements.
- Path following and crack propagating are treated simultaneously without a special strategy.
- The Sherman-Morrison formula is used for implementation of the solution process. The coding efforts are reduced.
- The stiffness factor of the arc-length constraint is obtained during, rather than before, the solution process. Hence, the derivative of the state variable with respect to the load control parameter is not needed.

With this approach, the dissipation path can be followed from the appearance of the first crack until the collapse of the structure. To assess the robustness of the approach, in most examples irregular meshes, generated by the Gmsh software [20] are considered.

The paper is organized as follows: In Section 2, the CEM is introduced briefly. The traction-separation law is presented and the numerical formulation is provided. In Section 3, the direct dissipation-based arc-length approach, including its constraint equation and the detailed numerical procedures, based on the Sherman-Morrison formula, are presented. In Section 4, numerical examples are given to demonstrate the robustness and the reliability of the approach. Finally, Section 5 contains concluding remarks.

2. The Cracking Elements Method

The CEM was first presented in Ref. [11]. It is based on the strong discontinuity embedded approach of the statically optimal symmetric formulation (SDA-SOS) as a standard Galerkin-based numerical approach [21]. As pointed out in Ref. [21], when using elements with non-linear interpolation of the displacement and proper equivalent crack area, stress-locking of the original SDA-SOS is automatically eliminated. This work is embedded in the framework of the recently presented Global Cracking Elements Method [19]. In this Section a brief introduction to the CEM is provided. Most of the symbols are the same as those used in Ref. [19].

2.1. Traction-separation law

The mixed-mode traction-separation law [22,23], where the normal and the shear directions of the crack surface are defined by the unit vectors $\mathbf{n} = [n_x, n_y]^T$ and $\mathbf{t} = [t_x, t_y]^T$, is used in this work. The crack openings along these two directions are denoted as $\zeta = [\zeta_n, \zeta_t]^T$, and the traction across the two crack surfaces is denoted as $\mathbf{T} = [T_n, T_t]^T$; see Fig. 1.

Based on ζ , \mathbf{T} is obtained as

$$\mathbf{T} = \begin{bmatrix} T_n \\ T_t \end{bmatrix} = \frac{T_{eq}}{\zeta_{eq}} \begin{bmatrix} \zeta_n \\ \zeta_t \end{bmatrix},$$

with

$$\zeta_{eq} = \sqrt{\zeta_n^2 + \zeta_t^2}$$

and

$$T_{eq}(\zeta_{eq}) = \begin{cases} L_1(\zeta_{eq}) = \frac{f_t}{\zeta_0} \zeta_{eq} & \text{for loading if } \zeta_{eq} \leq \zeta_0, \\ L_2(\zeta_{eq}) = f_t \exp\left[-\frac{f_t(\zeta_{eq} - \zeta_0)}{G_f - G_{f,0}}\right] & \text{for loading if } \zeta_{eq} > \zeta_0, \\ U(\zeta_{eq}) = \frac{T_{mx}}{\zeta_{mx}} \zeta_{eq} & \text{for unloading/reloading.} \end{cases} \quad (1)$$

In Eq. (1), f_t denotes the uniaxial tensile strength and G_f stands for the fracture energy. $G_{f,0}$ denotes the threshold value of G_f , assuming $G_{f,0} = 0.01G_f$. ζ_0 is the corresponding threshold opening, with $\zeta_0 = 2G_{f,0}/f_t$, which is a relatively small value. ζ_{mx} stands for the maximum opening that the crack has ever experienced. This value is updated at the end of each load step if $\zeta_{mx} > \zeta_0$. $T_{mx} = L_2(\zeta_{mx})$ is the corresponding traction. Additional details can be found in Ref. [19].

ζ_0 can be considered as a penalty, which was also used by such as XFEM [22] and interface element model [24]. In the early version of the CEM [11,12], $\zeta_0 = 0$ was set and the cracked elements can only get softer. This may lead to i) spurious cracking region which needs “spreading checking” procedure [11] for compensation and ii) cracks compete to open that some cracks get opened at odd Newton-Raphson (N-R) iteration step and closed at even N-R iteration step since the residual strengths of cracked elements are generally similar. After introducing $\zeta_0 > 0$ in Ref. [19], the “spreading checking” procedure is removed and the numerical stability is enhanced that the total N-R iteration steps are greatly reduced.

Consequently, $\mathbf{D} = \partial\mathbf{T}/\partial\zeta$ is obtained as

$$\mathbf{D} = \begin{bmatrix} \partial T_n / \partial \zeta_n & \partial T_n / \partial \zeta_t \\ \partial T_t / \partial \zeta_n & \partial T_t / \partial \zeta_t \end{bmatrix} = \begin{cases} \begin{bmatrix} \frac{f_t}{\zeta_0} & \begin{bmatrix} 1 & 0 \\ 0 & 1 \end{bmatrix} \end{bmatrix} & \text{for loading if } \zeta_{eq} \leq \zeta_0, \\ \begin{bmatrix} T_{eq} & \begin{bmatrix} \frac{\zeta_n^2}{\zeta_{eq}^2} + \frac{f_t \zeta_n^2}{G_f - G_{f,0}} - \zeta_{eq} & \frac{\zeta_n \zeta_t}{\zeta_{eq}} + \frac{f_t \zeta_n \zeta_t}{G_f - G_{f,0}} \\ \frac{\zeta_n \zeta_t}{\zeta_{eq}} + \frac{f_t \zeta_n \zeta_t}{G_f - G_{f,0}} & \frac{\zeta_t^2}{\zeta_{eq}^2} + \frac{f_t \zeta_t^2}{G_f - G_{f,0}} - \zeta_{eq} \end{bmatrix} \end{bmatrix} & \text{for loading if } \zeta_{eq} > \zeta_0, \\ \begin{bmatrix} T_{mx} & \begin{bmatrix} 1 & 0 \\ 0 & 1 \end{bmatrix} \\ \zeta_{mx} & \begin{bmatrix} 1 & 0 \\ 0 & 1 \end{bmatrix} \end{bmatrix} & \text{for unloading/reloading.} \end{cases} \quad (2)$$

Herein, an exponential law is used. However, other types of traction-separation laws, such as linear, bilinear, and hyperbolic ones, can also be implemented.

On the other hand, Eqs. (1) and (2) only consider the cases for crack openings as $\zeta_n \geq 0$. In the iteration, when $\zeta_n < 0$ happens, a large contact traction is needed for avoiding intrusion. We use the following equation for obtaining \mathbf{T} with $\zeta_n < 0$

$$\mathbf{T} = \begin{bmatrix} T_n \\ T_t \end{bmatrix} = \frac{E}{l_c} \begin{bmatrix} \zeta_n \\ \beta \zeta_t \end{bmatrix} \quad (3)$$

where E is the elastic modulus. l_c is the equivalent characteristic length which will be discussed in the next section. β is a friction factor and $\beta = 0.7$ is assumed in this work. Correspondingly, \mathbf{D} is obtained by

$$\mathbf{D} = \frac{E}{l_c} \begin{bmatrix} 1 & 0 \\ 0 & \beta \end{bmatrix}. \quad (4)$$

Herein, we would like to emphasize Eq. (3) can help to avoid intrusion in the simulation, but it is not designed for capturing shear damage in this work, which is still under investigation.

2.2. The global formulation

Considering a domain Ω separated by a discontinuity \mathbf{L} into Ω^+ and Ω^- , a localized subdomain Ω_ϕ is introduced to avoid singularity, leading to the displacement field of Ω

$$\mathbf{u}(\mathbf{x}) = \bar{\mathbf{u}}(\mathbf{x}) + [H_s(\mathbf{x}) - \phi(\mathbf{x})][\mathbf{u}]. \quad (5)$$

where $\bar{\mathbf{u}}(\mathbf{x})$ is the regular part, $H_s(\mathbf{x})$ is the Heaviside function, and $\phi(\mathbf{x})$ is a smooth function with $\phi(\mathbf{x}) \in [0, 1]$, see Fig. 2. Determination of \mathbf{n} and \mathbf{t} is not related to the formulation of the CEM, and these vectors are assumed to be known.

The notion of enhanced assumed strains (EAS) [25] is used in the CEM. EAS is a simple model for bridging the crack opening to the strains, which was also used by some other SDAs [26,27] and XFEMs [28]. The total strain $\hat{\boldsymbol{\varepsilon}}$ in the domain $\Omega(\mathbf{x})$, experiencing cracking, consists of the elastic strain $\bar{\boldsymbol{\varepsilon}}$ and the enhanced strain $\tilde{\boldsymbol{\varepsilon}}$, i.e.

$$\underbrace{\hat{\boldsymbol{\varepsilon}}(\mathbf{x}) = \nabla^S \bar{\mathbf{u}}(\mathbf{x})}_{\text{total strain}} = \underbrace{\bar{\boldsymbol{\varepsilon}}(\mathbf{x})}_{\text{elastic strain}} + \underbrace{[(\mathbf{n} \otimes \nabla \phi)^S \zeta_n(\mathbf{x}) + (\mathbf{t} \otimes \nabla \phi)^S \zeta_t(\mathbf{x})]}_{\text{enhanced strain } \tilde{\boldsymbol{\varepsilon}}}, \quad (6)$$

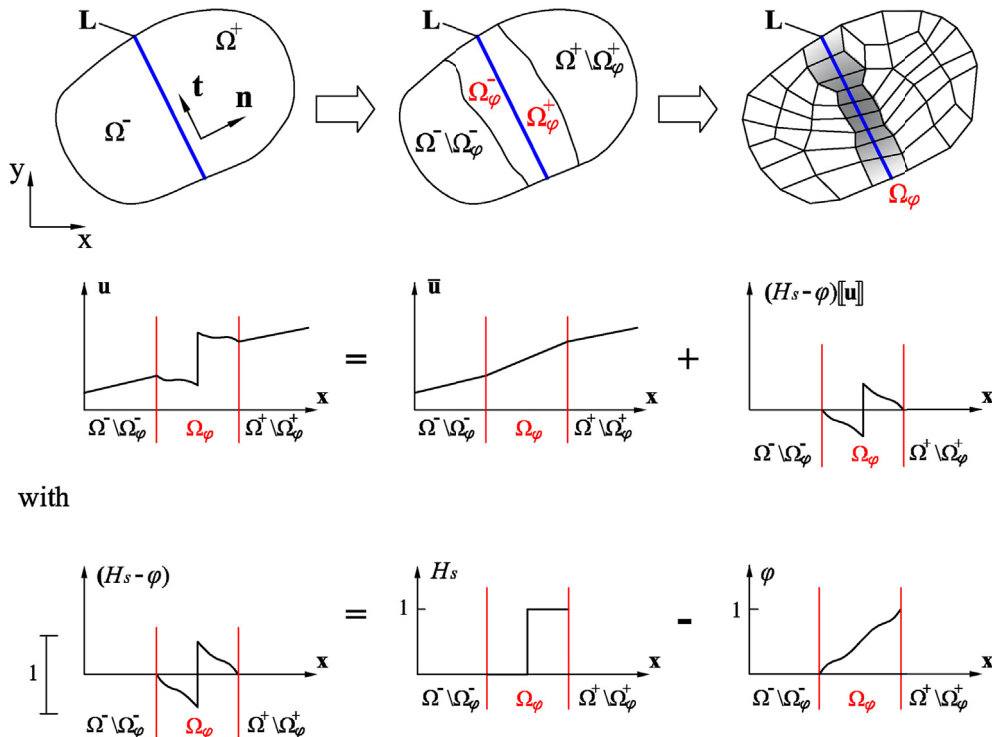


Fig. 2. Ω and its displacement field.

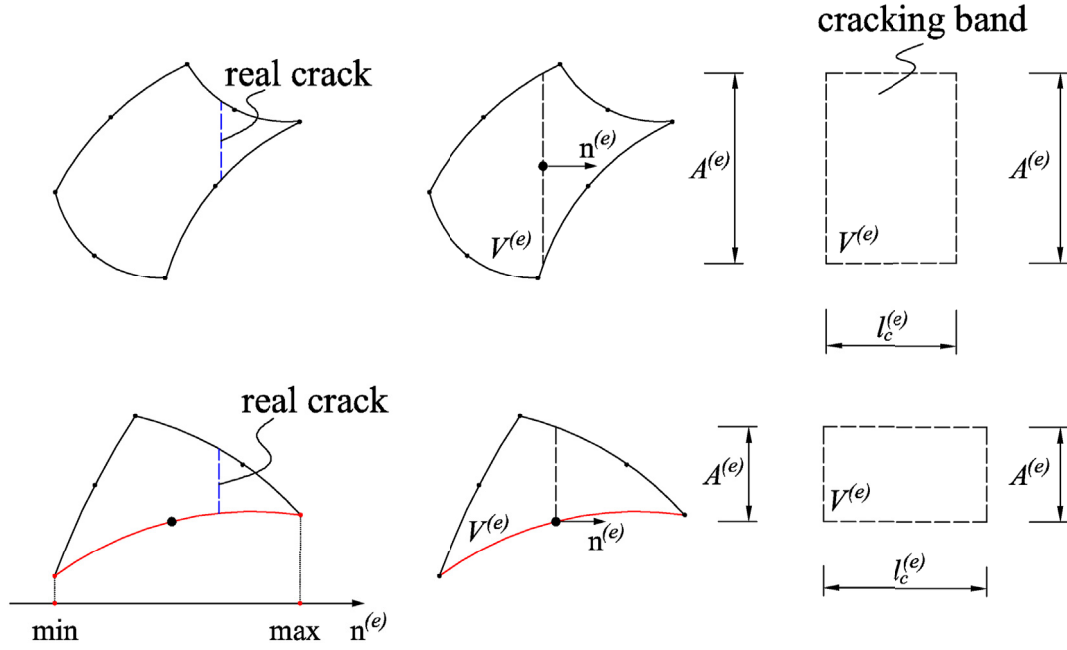


Fig. 3. Relationships between l_c , $V^{(e)}$ and $A^{(e)}$ of Q8 and T6.

where $\nabla\phi$ is a vector of dimension “length⁻¹” that links the crack opening to the enhanced strain. $\nabla\phi = \mathbf{n}/l_c$ [21], where l_c corresponds to the classic characteristic length [29,30]. In the framework of the finite element method (FEM), Eq. (6) yields

$$\bar{\boldsymbol{\varepsilon}}^{(e)} \approx \underbrace{\sum_{i=1}^n (\nabla N_i^{(e)} \otimes \mathbf{u}_i)^S}_{\hat{\boldsymbol{\varepsilon}}^{(e)}} - \underbrace{\frac{1}{l_c^{(e)}} \left[(\mathbf{n}^{(e)} \otimes \mathbf{n}^{(e)}) \zeta_n^{(e)} + (\mathbf{n}^{(e)} \otimes \mathbf{t}^{(e)}) \zeta_t^{(e)} \right]}_{\tilde{\boldsymbol{\varepsilon}}^{(e)}} \quad (7)$$

where $(\cdot)^S$ denotes the symmetric part of the tensor [26], while $(\cdot)^{(e)}$ refers to the respective quantity for element e . Herein, $[\zeta_n^{(e)}, \zeta_t^{(e)}]$ indicates that the crack openings are constant inside the element. n denotes the number of nodes of a finite element. The CEM has been proven to be reliable for implementations with 8-node quadrilateral elements (Q8, $n = 8$) [11,12] and 6-node triangular elements (T6, $n = 6$) [31]. Based on the conservation of energy, the element-dependent $l_c^{(e)}$ is obtained as $V^{(e)}/A^{(e)}$, where $V^{(e)}$ denotes the volume of element e and $A^{(e)}$ stands for the surface area of an equivalent crack parallel to the real crack. Here, the determination of $A^{(e)}$ for Q8 and T6 is slightly different insofar as the equivalent crack passes through the center point of Q8, but through the midpoint of one edge of T6; see Fig. 3. More details can be found in Refs. [19,31].

For quasi-static loading, the global momentum balance and local traction-stress balance [11,21] equations are given as

$$\begin{cases} \nabla \cdot \boldsymbol{\sigma} - \mathbf{F} = \mathbf{0} & \forall e \in \Omega, \\ \left[\begin{matrix} (\mathbf{n}^{(e)} \otimes \mathbf{n}^{(e)}) : \boldsymbol{\sigma}^{(e)} \\ (\mathbf{n}^{(e)} \otimes \mathbf{t}^{(e)}) : \boldsymbol{\sigma}^{(e)} \end{matrix} \right] - \mathbf{T}^{(e)} = \mathbf{0} & \forall e \in \Omega_\phi. \end{cases} \quad (8)$$

where \mathbf{F} denotes the loading force and $\boldsymbol{\sigma}^{(e)} = \mathbf{C}^{(e)} : \bar{\boldsymbol{\varepsilon}}^{(e)}$, with $\mathbf{C}^{(e)}$ standing for the elasticity tensor. As shown in Fig. 2, Ω_ϕ is the domain composed by the elements experiencing cracking. We want to emphasize the local traction-stress balance equation is defined on the local $\mathbf{n} - \mathbf{t}$ coordination system and the second order tensors $(\mathbf{n}^{(e)} \otimes \mathbf{n}^{(e)})$ and $(\mathbf{n}^{(e)} \otimes \mathbf{t}^{(e)})$ play the role for transformation. Hence no extra rota-

tional procedure is needed.

The CEM was reformulated in matrix form in Ref. [19], which is very simple and convenient. The symmetric second- and fourth-order tensors are represented in vector and matrix form, respectively, using Voigt’s notation [32]. The displacement vector is given as $\mathbf{U}^{(e)} = [\mathbf{u}_1^{(e)} \dots \mathbf{u}_n^{(e)}]^T$. The total strain is obtained as $\hat{\boldsymbol{\varepsilon}}^{(e)} = \mathbf{B}^{(e)} \mathbf{U}^{(e)}$, where $\mathbf{B}^{(e)}$ is defined as

$$\mathbf{B}^{(e)} = \begin{bmatrix} \mathbf{B}_1^{(e)} & \dots & \mathbf{B}_n^{(e)} \end{bmatrix},$$

with

$$\mathbf{B}_i^{(e)} = \begin{bmatrix} \frac{\partial N_i^{(e)}}{\partial x} & 0 \\ 0 & \frac{\partial N_i^{(e)}}{\partial y} \\ \frac{\partial N_i^{(e)}}{\partial y} & \frac{\partial N_i^{(e)}}{\partial x} \end{bmatrix}, \quad i = 1 \dots n. \quad (9)$$

Next, based on Eq. (7), the following matrix is introduced:

$$\mathbf{B}_\zeta^{(e)} = \frac{-1}{l_c^{(e)}} \begin{bmatrix} \mathbf{n}^{(e)} \otimes \mathbf{n}^{(e)} \\ (\mathbf{n}^{(e)} \otimes \mathbf{t}^{(e)})^S \end{bmatrix}^T = \frac{-1}{l_c^{(e)}} \begin{bmatrix} n_x^{(e)} \cdot n_x^{(e)} & n_x^{(e)} \cdot t_x^{(e)} \\ n_y^{(e)} \cdot n_y^{(e)} & n_y^{(e)} \cdot t_y^{(e)} \\ 2 n_x^{(e)} \cdot n_y^{(e)} & n_x \cdot t_y^{(e)} + n_y^{(e)} \cdot t_x^{(e)} \end{bmatrix}. \quad (10)$$

With the help of the matrices $\mathbf{B}^{(e)}$ and $\mathbf{B}_\zeta^{(e)}$, Eq. (8) is rewritten as

$$\begin{cases} \int_{\Omega} \left[(\mathbf{B}^{(e)})^T \mathbf{C}^e \bar{\boldsymbol{\varepsilon}}^{(e)} - \mathbf{F}^{(e)} \right] dx = \mathbf{0}, \\ -l_c (\mathbf{B}_\zeta^{(e)})^T \boldsymbol{\sigma}^{(e)} - \begin{bmatrix} T_n^{(e)} \\ T_t^{(e)} \end{bmatrix} = \mathbf{0}, \forall e \text{ experiencing cracking.} \end{cases} \quad (11)$$

where \mathbf{C}^e denotes the matrix form of $\mathbf{C}^{(e)}$.

Meanwhile, Eq. (7) gives

$$\bar{\boldsymbol{\varepsilon}}^{(e)} = \bar{\boldsymbol{\varepsilon}}^{(e),1} = \begin{bmatrix} \mathbf{B}^{(e),1} & \mathbf{B}_\zeta^{(e)} \end{bmatrix} \begin{bmatrix} \mathbf{U}^{(e)} \\ \boldsymbol{\zeta}^{(e)} \end{bmatrix}. \quad (12)$$

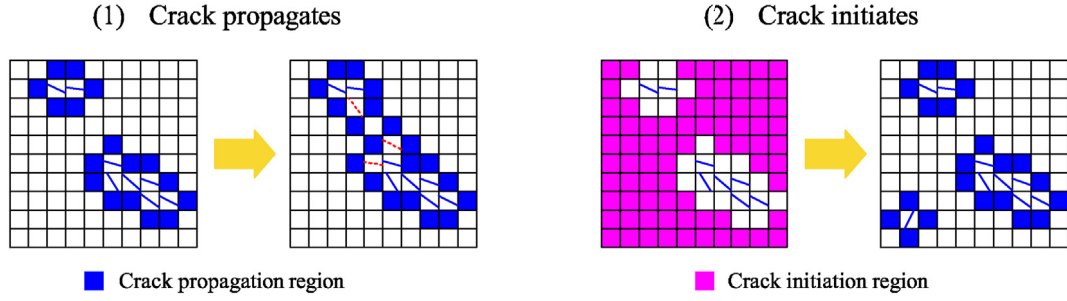


Fig. 4. Crack propagation and initiation regions.

where $\mathbf{B}^{(e),1}$ stands for $\mathbf{B}^{(e)}$, evaluated at the center Gauss point (center representation) [19].

With Newton-Raphson method, for the iteration step l at load step i the element-related incremental relation is obtained as follows:

$$\begin{bmatrix} \mathbf{U}_{i,l}^{(e)} \\ \zeta_{i,l}^{(e)} \end{bmatrix} = \underbrace{\begin{bmatrix} \mathbf{U}_{i-1}^{(e)} \\ \zeta_{i-1}^{(e)} \end{bmatrix} + \begin{bmatrix} \Delta \mathbf{U}_{l-1}^{(e)} \\ \Delta \zeta_{l-1}^{(e)} \end{bmatrix}}_{\text{known}} + \underbrace{\begin{bmatrix} \Delta \Delta \mathbf{U}^{(e)} \\ \Delta \Delta \zeta^{(e)} \end{bmatrix}}_{\text{unknown}}. \quad (13)$$

In Eq. (13), $\Delta(\cdot)$ denotes an increment of the corresponding value at the preceding load step, $i - 1$, while $\Delta\Delta(\cdot)$ stands for an increment of the value at the last N-R iteration step, $l - 1$.

After linearization, the element-related balance equation, deduced in Ref. [19], is obtained as follows:

$$\mathbf{K}_{sym}^{(e)} \begin{bmatrix} \Delta \Delta \mathbf{U}^{(e)} \\ \Delta \Delta \zeta^{(e)} \end{bmatrix} = \left[\mathbf{F} - \frac{V^{(e)}}{l_c^{(e)}} \mathbf{T}^{(e)} \right] - \mathbf{K}^{(e)} \begin{bmatrix} \mathbf{U}_{i-1}^{(e)} + \Delta \mathbf{U}_{l-1}^{(e)} \\ \zeta_{i-1}^{(e)} + \Delta \zeta_{l-1}^{(e)} \end{bmatrix},$$

with

$$\mathbf{K}^{(e)} = \begin{bmatrix} \int_{(e)} (\mathbf{B}^{(e)})^T \mathbf{C}^{(e)} (\mathbf{B}^{(e),1}) dx & \int_{(e)} (\mathbf{B}^{(e)})^T \mathbf{C}^{(e)} \mathbf{B}_\zeta^{(e)} dx \\ V^{(e)} (\mathbf{B}_\zeta^{(e)})^T \mathbf{C}^{(e)} (\mathbf{B}^{(e),1}) & V^{(e)} (\mathbf{B}_\zeta^{(e)})^T \mathbf{C}^{(e)} \mathbf{B}_\zeta^{(e)} \end{bmatrix} \quad (14)$$

and

$$\mathbf{K}_{sym}^{(e)} = \int_{(e)} \begin{bmatrix} \mathbf{B}^{(e)} & \mathbf{B}_\zeta^{(e)} \end{bmatrix}^T \mathbf{C}^{(e)} \begin{bmatrix} \mathbf{B}^{(e)} & \mathbf{B}_\zeta^{(e)} \end{bmatrix} dx + \begin{bmatrix} \mathbf{0} & \mathbf{0} \\ \mathbf{0} & \frac{V^{(e)}}{l_c^{(e)}} \mathbf{D}^{(e)} \end{bmatrix}.$$

While $\mathbf{K}^{(e)}$ is an unsymmetric matrix with many zero elements, $\mathbf{K}_{sym}^{(e)}$ is a symmetric matrix. \mathbf{T} and \mathbf{D} are the tractions and stiffness based on the traction-separation law, obtained by Eqs. (1)–(4). On [33], we uploaded our Fortran source codes for building Eq. (14) of the Q8 and T6 elements.

In this work a dynamic element-related enrichment version of the CEM is used [34]. $\int_{(e)} (\cdot) dx$ indicates the integral of functions over element e . Once element e experiences cracking, the additional degree of freedom, $\zeta^{(e)}$, is introduced as a new global unknown.

2.3. Crack propagation

The CEM does not require continuous crack paths. Instead of them, it uses cracking segments. This leads to the distinguishing feature that the CEM does not need a crack tracking strategy which predicts the crack orientation and assures the crack connectivity. Instead, only the local orientation \mathbf{n} of the crack needs to be known. $\mathbf{n}^{(e)}$ depends only on $\hat{\boldsymbol{\varepsilon}}^{(e)}$ and is not related to any other element, making determination of $\mathbf{n}^{(e)}$ simple and efficient. It is assumed to be the first unit eigenvector of the total strain $\hat{\boldsymbol{\varepsilon}}$ at the center point, i.e.,

$$\hat{\boldsymbol{\varepsilon}}^{(e)} \cdot \mathbf{n}^{(e)} - \hat{\boldsymbol{\varepsilon}}_1^{(e)} \cdot \mathbf{n}^{(e)} = \mathbf{0},$$

where

$$\hat{\boldsymbol{\varepsilon}}^{(e)} = \sum_{i=1}^n (\nabla N_i^{(e)} \otimes \mathbf{u}_i)^S = \begin{bmatrix} \hat{\boldsymbol{\varepsilon}}_x^{(e)} & \hat{\gamma}_{xy}^{(e)} / 2 \\ \hat{\gamma}_{xy}^{(e)} / 2 & \hat{\boldsymbol{\varepsilon}}_y^{(e)} \end{bmatrix}, \quad (15)$$

and

$$\hat{\boldsymbol{\varepsilon}}_1^{(e)} = \frac{\hat{\boldsymbol{\varepsilon}}_x^{(e)} + \hat{\boldsymbol{\varepsilon}}_y^{(e)} + \sqrt{(\hat{\boldsymbol{\varepsilon}}_x^{(e)} - \hat{\boldsymbol{\varepsilon}}_y^{(e)})^2 + (\hat{\gamma}_{xy}^{(e)})^2}}{2}.$$

The elements are cracking one after another. All elements in the whole domain are classified into two regions: i) crack propagation region, ii) crack initiation region, based on whether the element share at least one edge with a cracked element, see Fig. 4. Then crack propagation region is always checked first, then, crack initiation region is considered, by the following strategy for identifying the next cracking element:

find $\max \{ \varphi_{RK}^{(e)} \}$ with

$$\varphi_{RK}^{(e)} = (\mathbf{n}^{(e)} \otimes \mathbf{n}^{(e)}) : \mathbf{C}^{(e)} : \hat{\boldsymbol{\varepsilon}}^{(e)} - f_t^{(e)}$$

and $\varphi_{RK}^{(e)} > 0$,

where $\varphi_{RK}^{(e)} > 0$ can be considered as a Rankine-like criterion, which was also considered by the CPM in Ref. [14]. The loss of hyperbolicity criterion proposed in Ref. [14] is still under investigation. Once $\varphi_{RK}^{(e)} < 0$ for all non-cracked elements, the iteration stops. This strategy was first presented in Ref. [11]. A detailed flowchart was provided in Ref. [19]. On the other hand, the element experiencing highest $\varphi_{RK}^{(e)}$ shall be given priority for cracking. Some researchers may point out because the tip element should naturally experience highest $\varphi_{RK}^{(e)}$ when the crack propagates. It is unnecessary to distinguish the two regions. However, we want to emphasize that $\varphi_{RK}^{(e)}$ is obtained on the center point of “ e ”. When the sizes of elements have great differences, smaller elements are prone to crack, which may lead to unexpected spurious cracking. Hence, we conduct crack propagation and initiation in two steps.

3. Direct dissipation-based arc-length approach

3.1. Basics

For a deformed body with cohesive discontinuities, the mechanical energy Ψ (see Refs. [22,35]) is given as

$$\Psi = I + E - W, \quad (16)$$

where I is the elastic strain energy (internal energy), E is the dissipated energy, and W is the work done by the applied forces.

Most energy-based arc-length methods use $W - I$ and not E as the state variable [5]. This is reasonable since $W - I$ is related to the displacements and E is related to the crack openings. However, a structure

with propagating cracks is not a conservative system. When cracks are propagating, Ψ is a function of the crack direction and the surface area, and it is not zero [35]. The crack direction and the surface are changing continuously during the loading process [36]. For $\Psi > 0$, $W - I < 0$ may occur. In this case, $W - I$ cannot be used as the state variable. Moreover, the difference between $W - I$ and E is further affected by the numerical error in the iteration step. This difference is more obvious for crack-opening based models than for damage-degree based models, because crack openings are reversible and without upper bounds, whereas the damage degree is irreversible and bounded.

The CEM is a crack-opening based model [17]. For better numer-

ical stability, E is used directly as the state variable of the arc-length method. For convenience, the following global vectors are defined:

$$\mathbf{Z} = \cup \zeta^{(e)} \quad \text{and} \quad \frac{V}{l_c} \mathbf{T} = \cup \left(\frac{V^{(e)}}{l_c^{(e)}} \mathbf{T}^{(e)} \right), \quad (17)$$

where $\cup(\cdot)$ denotes the assemblage of the element matrix or vector to the global form. Then, considering Eqs. (13) and (14), by means of a forward Euler discretization, the incremental dissipated energy at load step i is obtained as

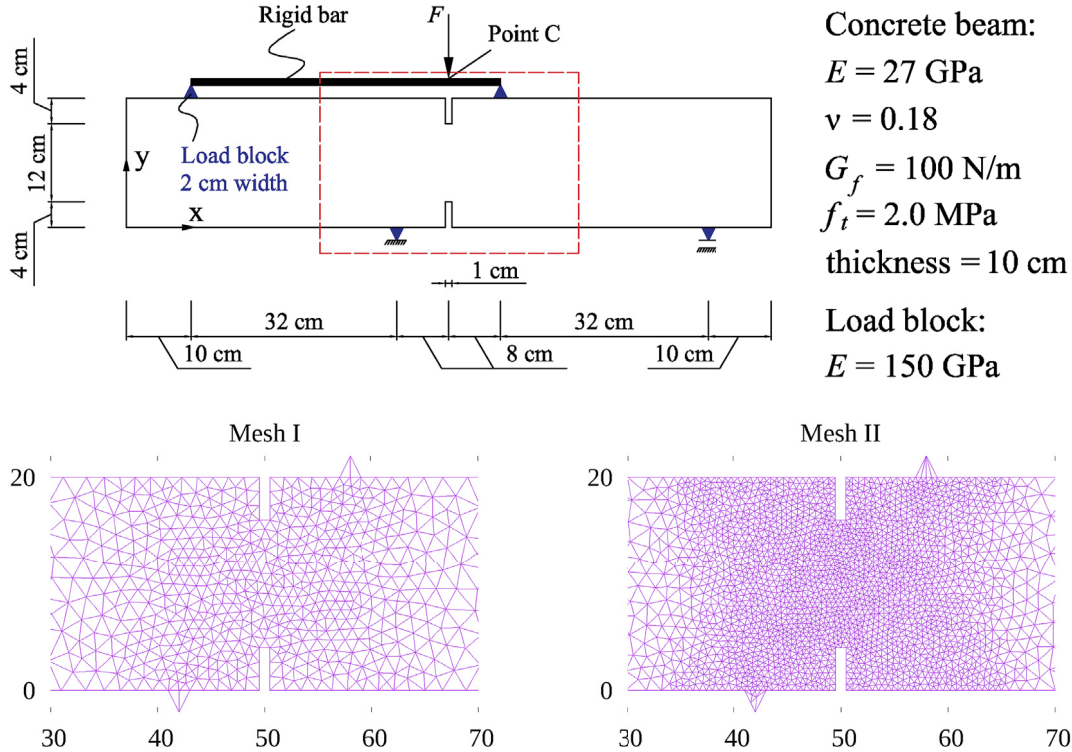


Fig. 5. Double-notched four-point bending test: model and material.

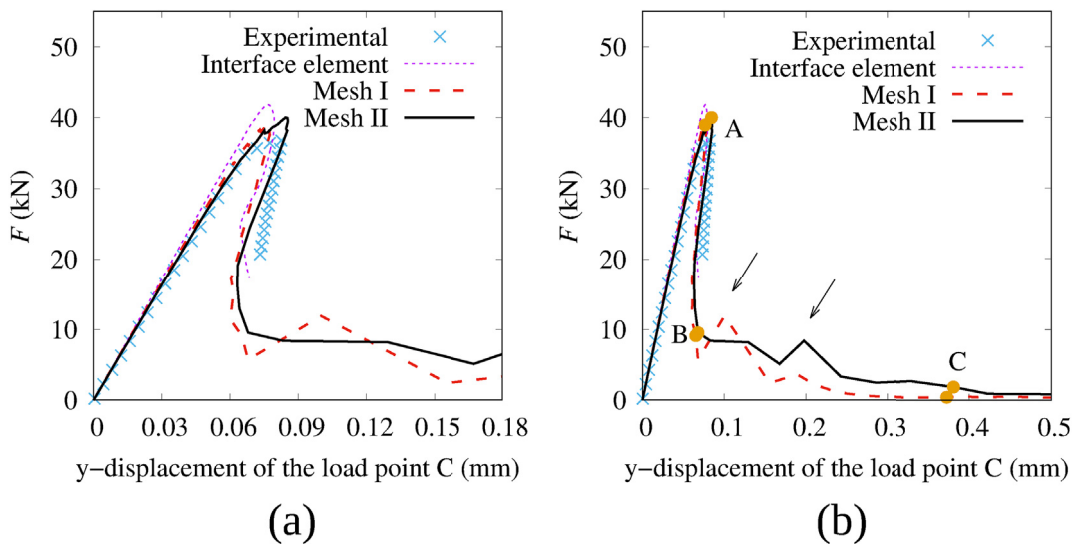


Fig. 6. Double-notched four-point bending test: force-displacement curves (a) early stage, (b) numerical results compared to the experimental results given in Ref. [42] and the numerical results given in [46].

$$\Delta E_i = \frac{1}{2} \left[\Delta \mathbf{Z}_i \left(\frac{\mathbf{V}}{l_c} \mathbf{T}^T \right)_{i-1} + \mathbf{Z}_{i-1} \Delta \left(\frac{\mathbf{V}}{l_c} \mathbf{T}^T \right)_i \right] \stackrel{!}{=} a, \tag{18}$$

where

$$\Delta \left(\frac{\mathbf{V}}{l_c} \mathbf{T}^T \right)_i = \left(\frac{\mathbf{V}}{l_c} \mathbf{T}^T \right)_i - \left(\frac{\mathbf{V}}{l_c} \mathbf{T}^T \right)_{i-1},$$

which is used as the arc-length constraint, where a is the prescribed arc-length. a is determined at the beginning of every load step, based on the residual dissipated energy of the system. In general, a is taken as 1% of the residual dissipated energy.

3.2. Formulation

Similar to Eq. (17), the following global matrices and vectors are defined:

$$\mathbf{K}_{sym} = \bigcup \mathbf{K}_{sym}^{(e)} \quad \text{and} \quad \mathbf{K} = \bigcup \mathbf{K}^{(e)} \tag{19}$$

$$\mathbf{U} = \bigcup \mathbf{U}^{(e)} \quad \text{and} \quad \mathbf{F} = \bigcup \mathbf{F}^{(e)} = \lambda \mathbf{f},$$

where λ is the unknown arc-length for controlling the load and \mathbf{f} is a prescribed reference load. Since in the equation only one λ appears, all live loads will be controlled by λ . If the live loads need to be controlled independently, more arc-lengths and constraints must be introduced. The state variables used by other constraints can refer to displacements, damage degrees, crack-opening and crack lengths. However, we would like to emphasize again. Considering monotonically loading conditions, when assuming the cracks can open and close, the monotonicity of some of these state variables cannot be assured, depending on different cases.

Based on Eq. (13), for iteration step l at load step i , the global arc-length based incremental relation is obtained as

$$\begin{bmatrix} \mathbf{U}_{i,l} \\ \mathbf{Z}_{i,l} \\ \lambda_{i,l} \end{bmatrix} = \underbrace{\begin{bmatrix} \mathbf{U}_{i-1} \\ \mathbf{Z}_{i-1} \\ \lambda_{i-1} \end{bmatrix}}_{\text{known}} + \underbrace{\begin{bmatrix} \Delta \mathbf{U}_{i-1} \\ \Delta \mathbf{Z}_{i-1} \\ \Delta \lambda_{i-1} \end{bmatrix}}_{\text{unknown}} + \begin{bmatrix} \Delta \Delta \mathbf{U} \\ \Delta \Delta \mathbf{Z} \\ \Delta \Delta \lambda \end{bmatrix}. \tag{20}$$

Stage A (deformation scale 1:200)



Stage B (deformation scale 1:50)



Stage C (deformation scale 1:20)

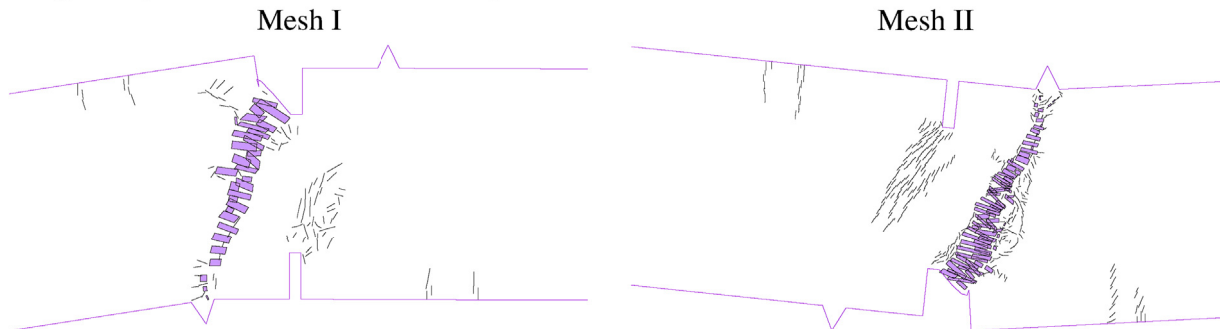


Fig. 7. Double-notched four-point bending test: crack opening plots ($\zeta_{eq} \geq 0$) with deformed boundaries.

Correspondingly, if $\Delta\Delta\lambda = 0$ for iteration step l at load step i , the following global balance equation is obtained after assemblage of the element balance equations, see Eq. (14):

$$\mathbf{K}_{sym} \begin{bmatrix} \Delta\Delta\mathbf{U} \\ \Delta\Delta\mathbf{Z} \end{bmatrix} = \begin{bmatrix} (\lambda_{i-1} + \Delta\lambda_{l-1})\mathbf{f} - \left(\frac{V}{l_c} \mathbf{T}\right)_{l-1} \\ \mathbf{0} \end{bmatrix} - \mathbf{K} \begin{bmatrix} \mathbf{U}_{i-1} + \Delta\mathbf{U}_{l-1} \\ \mathbf{Z}_{i-1} + \Delta\mathbf{Z}_{l-1} \end{bmatrix}. \quad (21)$$

When considering $\Delta\Delta\lambda$ and the constraint Eq. (18), the global balance equation is obtained as

$$\begin{bmatrix} \mathbf{K}_{sym} & -\mathbf{f} \\ \mathbf{0} & \mathbf{0} \\ \mathbf{0} & \left(\frac{V}{l_c} \mathbf{T}^T\right)_{i-1} \end{bmatrix} \begin{bmatrix} \Delta\Delta\mathbf{U} \\ \Delta\Delta\mathbf{Z} \\ \Delta\Delta\lambda \end{bmatrix} = \begin{bmatrix} R_U \\ R_Z \\ R_\lambda \end{bmatrix}, \quad (22)$$

where

$$\begin{bmatrix} R_U \\ R_Z \\ R_\lambda \end{bmatrix} = \begin{bmatrix} (\lambda_{i-1} + \Delta\lambda_{l-1})\mathbf{f} - \left(\frac{V}{l_c} \mathbf{T}\right)_{l-1} \\ \mathbf{0} \\ 2a \end{bmatrix} - \begin{bmatrix} \mathbf{K} & \mathbf{1} \\ \mathbf{1} & \mathbf{0} \\ \mathbf{0} & 2 \Delta E_{l-1} \end{bmatrix} \begin{bmatrix} \mathbf{U}_{i-1} + \Delta\mathbf{U}_{l-1} \\ \mathbf{Z}_{i-1} + \Delta\mathbf{Z}_{l-1} \\ \Delta E_{l-1} \end{bmatrix},$$

with

$$\Delta E_{l-1} = \frac{1}{2} \left[\Delta\mathbf{Z}_{l-1} \left(\frac{V}{l_c} \mathbf{T}^T\right)_{i-1} + \mathbf{Z}_{i-1} \Delta \left(\frac{V}{l_c} \mathbf{T}^T\right)_{l-1} \right]$$

and

$$\Delta \left(\frac{V}{l_c} \mathbf{T}^T\right)_{l-1} = \left(\frac{V}{l_c} \mathbf{T}^T\right)_{l-1} - \left(\frac{V}{l_c} \mathbf{T}^T\right)_{i-1}.$$

This equation raises two concerns:

- the coefficient matrix is unsymmetric;
- $k_\lambda = \partial\Delta E/\partial\lambda$ cannot be obtained analytically.

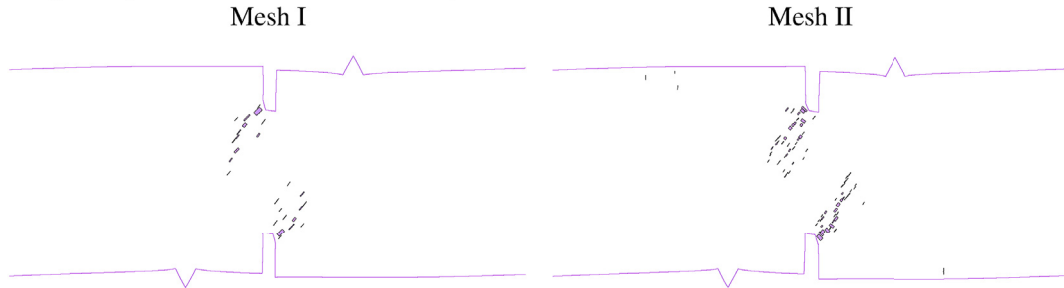
In the next Section, it will be shown that both concerns can be refuted by the Sherman-Morrison formula.

3.3. Sherman-Morrison formula

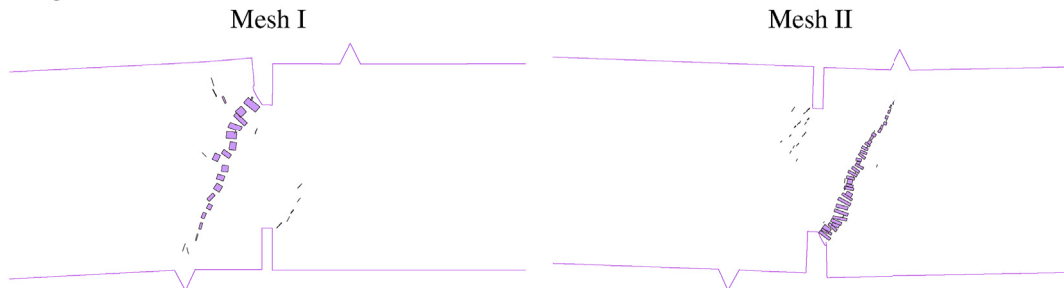
The Sherman-Morrison formula is widely used in arc-length methods [5] for separating the arc-length constraint from the global system to enable a more efficient solution. Based on this formula, two vectors are obtained by solving

$$\mathbf{K}_{sym} \begin{bmatrix} \Delta\Delta\mathbf{U}_I & \Delta\Delta\mathbf{U}_{II} \\ \Delta\Delta\mathbf{Z}_I & \Delta\Delta\mathbf{Z}_{II} \end{bmatrix} = \begin{bmatrix} R_U & -\mathbf{f} \\ R_Z & \mathbf{0} \end{bmatrix}. \quad (23)$$

Stage A (deformation scale 1:200)



Stage B (deformation scale 1:50)



Stage C (deformation scale 1:20)

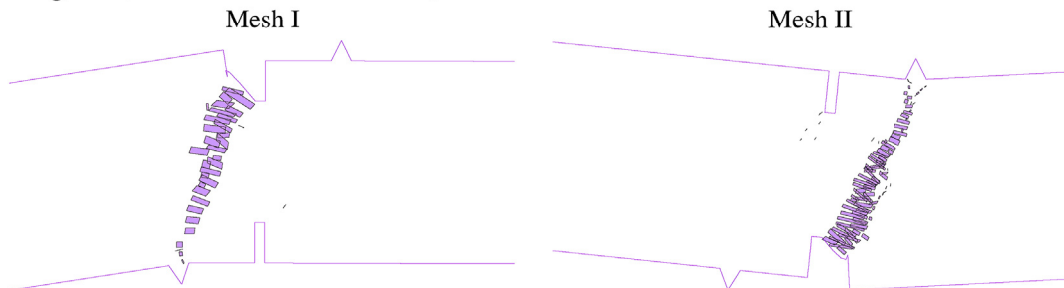


Fig. 8. Double-notched four-point bending test: crack opening plots ($\zeta_{eq} \geq \zeta_0$) with deformed boundaries.

This can be done by powerful linear solvers such as PARDISO [37,38] and MUMPS [39–41]. MUMPS 5.1.2 is used in this work. The symmetry of the original system is maintained. Thus, the first concern is refuted.

As regards the second concern, k_λ , by definition, is “the change of ΔE with respect of the unit increment f ”. Since $[\Delta\Delta\mathbf{U}_I, \Delta\Delta\mathbf{Z}_I]^T$ may be considered as the additional system response caused by $-f$, k_λ can be obtained by means of Eq. (18) as the difference between the trial values of ΔE_i . This involves the following steps:

obtain ΔE_I from \mathbf{Z}_{i-1} and $\Delta\mathbf{Z}_{i-1}$,

obtain ΔE_{II} from \mathbf{Z}_{i-1} and $\Delta\mathbf{Z}_{i-1} - \Delta\Delta\mathbf{Z}_{II}$,

then compute $k_\lambda \approx \Delta E_{II} - \Delta E_I$.

Notably, the procedure delineated above can be considered as a general strategy for obtaining k_λ , as used in most arc-length methods. This procedure is especially suitable for cases where the derivative of the state variable with respect to λ cannot be computed analytically.

Then, the final solution is obtained as

$$\begin{bmatrix} \Delta\Delta\mathbf{U} \\ \Delta\Delta\mathbf{Z} \\ \Delta\Delta\lambda \end{bmatrix} = \begin{bmatrix} \Delta\Delta\mathbf{U}_I \\ \Delta\Delta\mathbf{Z}_I \\ R_\lambda \end{bmatrix} - \frac{1}{S_{II} - k_\lambda} \begin{bmatrix} (S_I - R_\lambda) \Delta\Delta\mathbf{U}_{II} \\ (S_I - R_\lambda) \Delta\Delta\mathbf{Z}_{II} \\ -S_I + R_\lambda (1 + S_{II} - k_\lambda) \end{bmatrix}, \quad (24)$$



Fig. 9. Double-notched four-point bending test: crack paths comparing to the experimentally-obtained results provided in Ref. [42] and numerically-obtained results by remeshing strategy provided in [47].

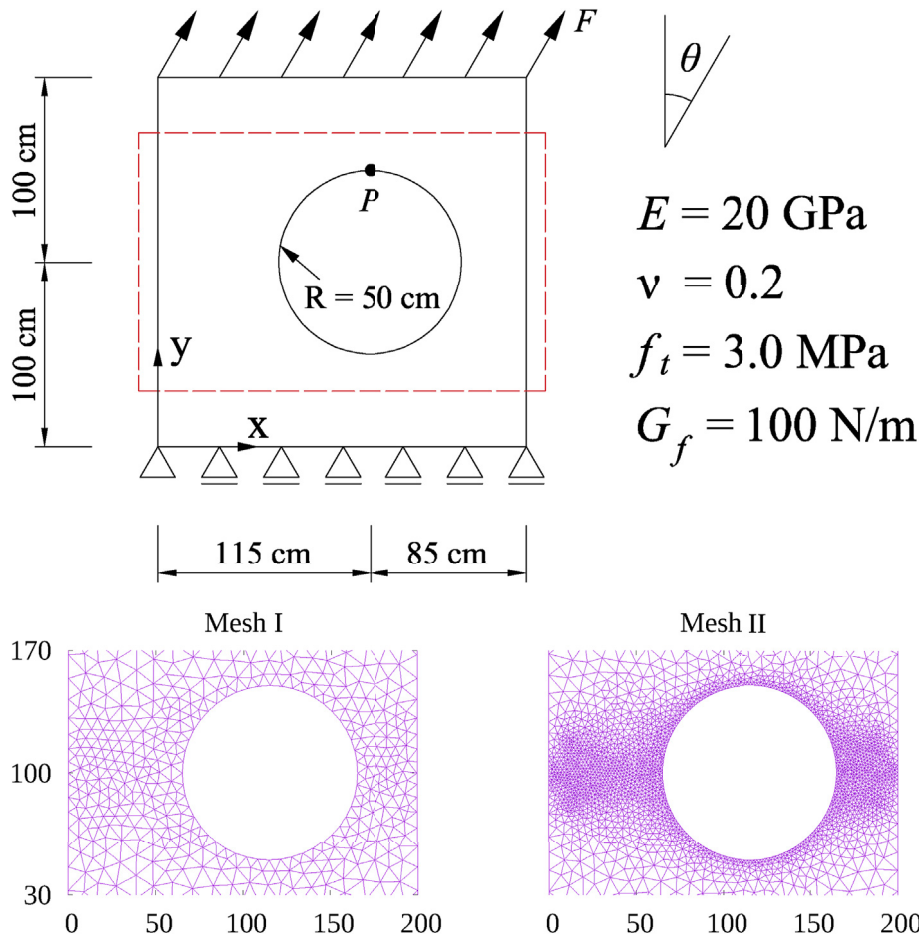


Fig. 10. Perforated plate with a hole: model and material.

where

$$S_I = \begin{bmatrix} \mathbf{0} & \left(\frac{V}{l_c} \mathbf{T}^T \right)_{i-1} \end{bmatrix} \begin{bmatrix} \Delta\Delta\mathbf{U}_I \\ \Delta\Delta\mathbf{Z}_I \end{bmatrix}$$

and

$$S_{II} = \begin{bmatrix} \mathbf{0} & \left(\frac{V}{l_c} \mathbf{T}^T \right)_{i-1} \end{bmatrix} \begin{bmatrix} \Delta\Delta\mathbf{U}_{II} \\ \Delta\Delta\mathbf{Z}_{II} \end{bmatrix}.$$

4. Numerical examples

The plane stress condition is assumed for all numerical examples.

4.1. Double-notched four-point bending test

The double-notched four-point bending test of a concrete beam [42], illustrated in Fig. 5, is a benchmark test investigated, e.g. in Refs.

[43–45]. Two meshes are considered with 1256 elements for Mesh I and 4605 elements for Mesh II. The load blocks in Fig. 5 are assumed to be unbreakable. Because of symmetry, two axisymmetric cracks begin to propagate in the early stage of loading, but only one crack is growing continuously until the beam fails. From this perspective, the path is difficult to trace via crack mouth opening, since both crack mouths open at the early stage of loading, but only one is opening continuously while the other changes from opening to closing.

The force-displacement curves shown in Fig. 6 are compared to the experimental results reported in Ref. [42] and to the numerical results given in Ref. [46], obtained with interface elements. In Fig. 6(b), there are two local peak loads marked by arrows. They are caused by the approach of the cracks to the unbreakable load blocks. Regarding $\zeta_{eq} \geq 0$, the crack opening plots with deformed boundaries at stages A, B, and C (see Fig. 6(b)) are shown in Fig. 7, which seem to show spurious cracking patterns. However, many cracks in Fig. 7 are no macro cracks, which will close with loading. When defining the cracks with $\zeta_{eq} > \zeta_0$ as macro cracks, the crack opening plots with deformed

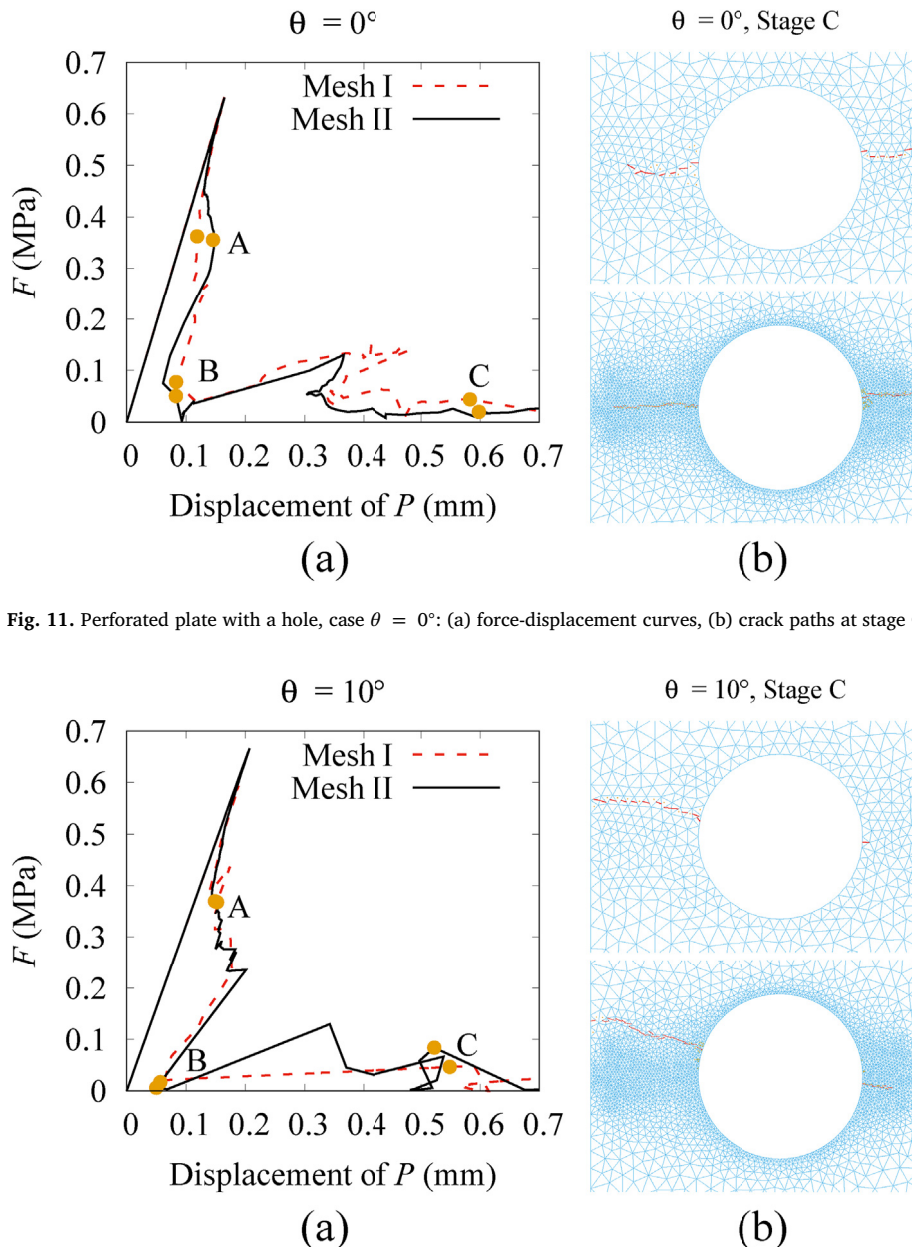


Fig. 11. Perforated plate with a hole, case $\theta = 0^\circ$: (a) force-displacement curves, (b) crack paths at stage C.

Fig. 12. Perforated plate with a hole, case $\theta = 10^\circ$: (a) force-displacement curves, (b) crack paths at stage C.

boundaries are shown in Fig. 8, indicating many cracks will get closed with further loadings. Fig. 9 shows the obtained crack paths, comparing to the experimental and numerical results provided in Refs. [42,47] respectively, indicating generally agreeable results. For both meshes, the dissipation-based arc-length approach captures the cracking process.

4.2. Perforated plate with a hole

A perforated plate with a hole is a benchmark test for checking arc-length methods [7,8,10,48]. It is an example for the absence of a crack mouth. The model and material are shown in Fig. 10. Two meshes are considered with 864 elements for Mesh I and 4569 elements for Mesh

II. The distributed force is applied at the top edge. The bottom edge is fixed in the y-direction direction. In this example, neither an interface element nor a prescribed crack path is used: all cracks initiate or propagate during the arc-length loading process. This is an advantage of the CEM.

Three cases with inclined angles $\theta = 0^\circ$, $\theta = 10^\circ$, and $\theta = 20^\circ$ of the distributed force are considered, leading to different force-displacement curves and crack paths, as shown in Figs. 11–13. For the cases with $\theta = 10^\circ$ and $\theta = 20^\circ$, oscillations of the force-displacement curves are observed. Crack opening and force-displacement curves are shown in Figs. 14–16. In case of $\theta = 0^\circ$, the crack starts to propagate on the right side of the hole. In case of $\theta = 10^\circ$ and $\theta = 20^\circ$, however,

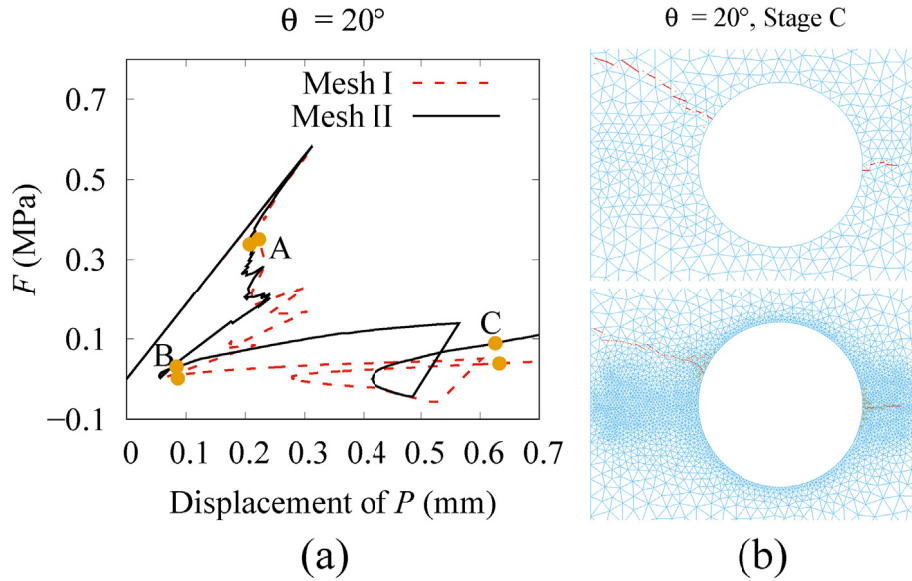


Fig. 13. Perforated plate with a hole, case $\theta = 20^\circ$: (a) force-displacement curves, (b) crack paths at stage C.

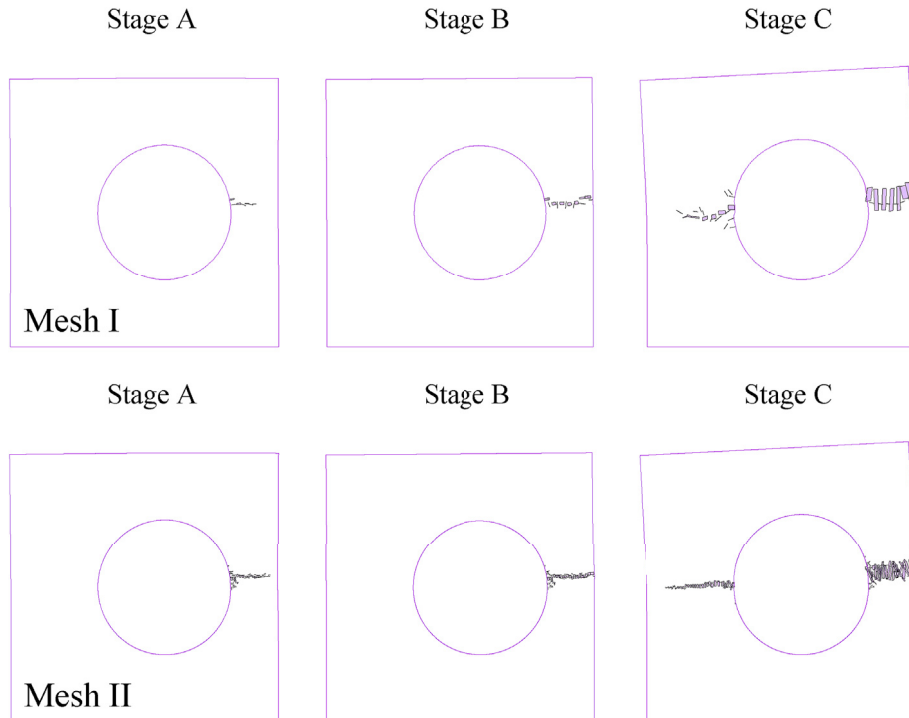


Fig. 14. Perforated plate with a hole, case $\theta = 0^\circ$: crack opening plots ($\zeta_{eq} \geq \zeta_0$) with deformed boundaries (scale = 1:100).

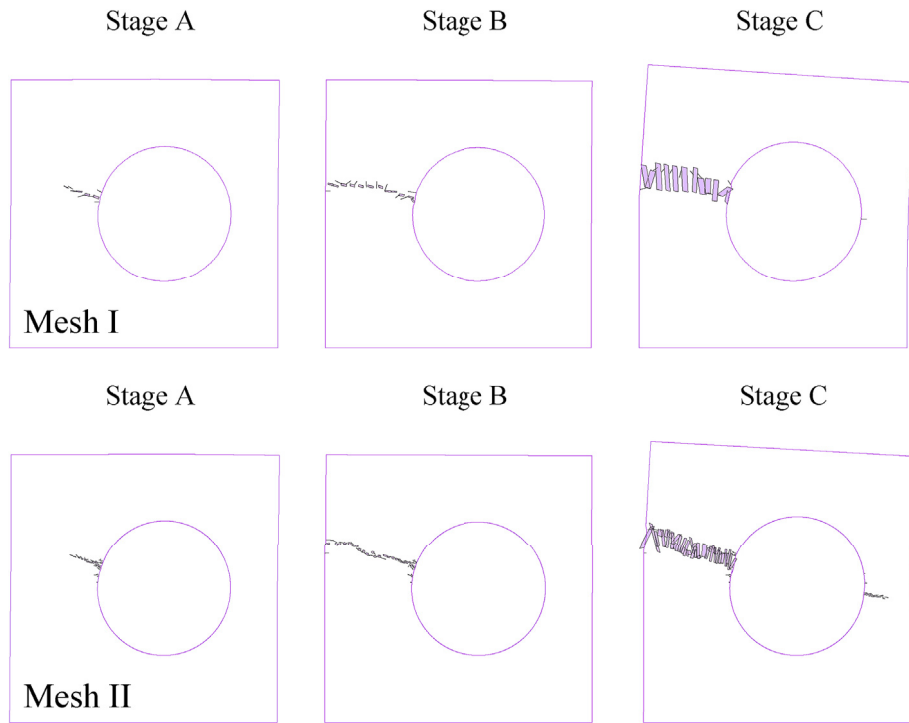


Fig. 15. Perforated plate with a hole, case $\theta = 10^\circ$: crack opening plots ($\zeta_{eq} \geq \zeta_0$) with deformed boundaries (scale = 1:100).

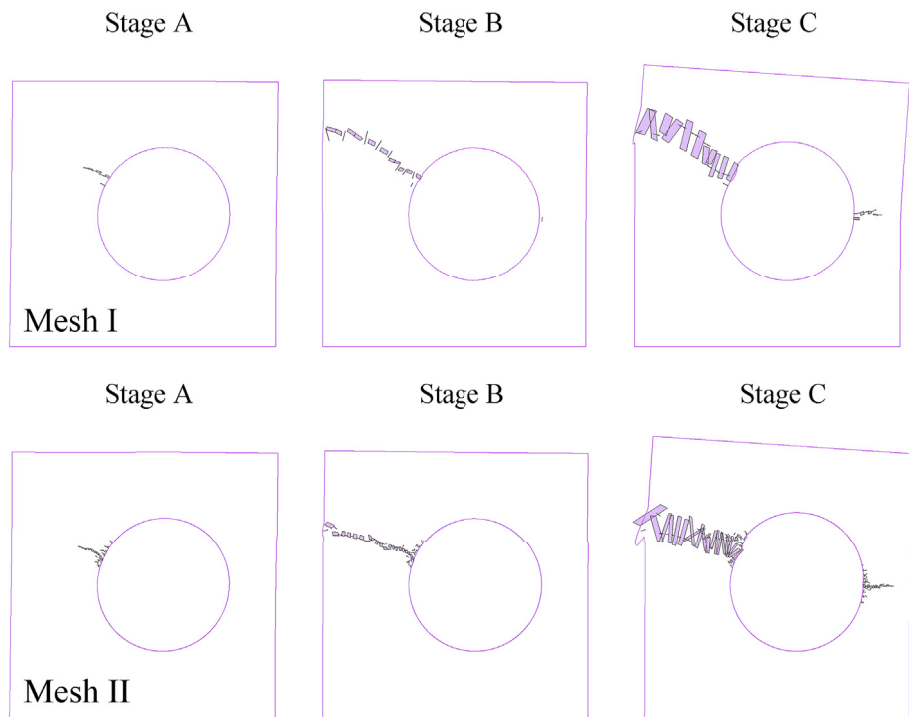


Fig. 16. Perforated plate with a hole, case $\theta = 20^\circ$: crack opening plots ($\zeta_{eq} \geq \zeta_0$) with deformed boundaries (scale = 1:100).

it starts propagating on the left side.

4.3. Specimen with multiple cracks

Quasi-brittle materials with multiple cracks, such as fractured rock, are common in geotechnical engineering practice. The cracking process of such materials usually exhibits a strong instability. In this example, a plate with ten initial cracks is considered. It was previously investigated

in Refs. [49–51] with XFEM and peridynamics. The model and material are shown in Fig. 17, where the width of all cracks is assumed to be 1 cm. The cracks are modelled explicitly in Meshes I (2548 elements) and II (12244 elements) and implicitly in Meshes III (900 elements) and IV (2500 elements). As a strong discontinuity embedded approach, implicit modelling of initial cracks is an advantage of the CEM over some other methods, such as the interface element methods.

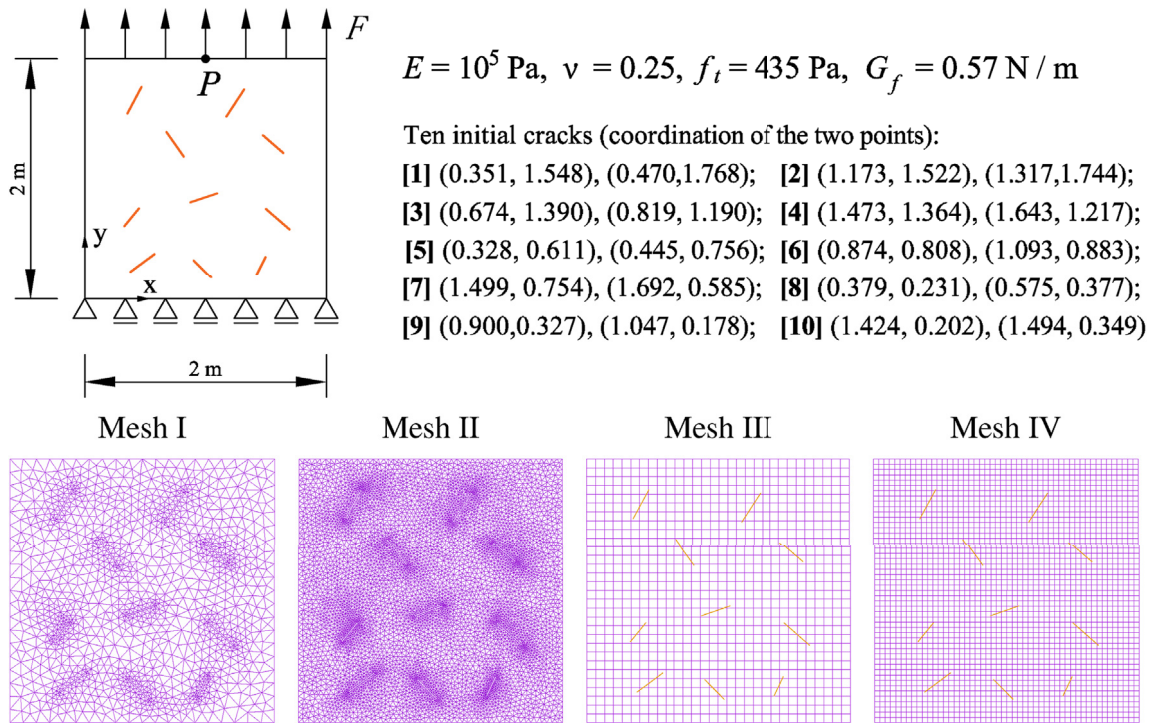


Fig. 17. Specimen with multiple cracks: model and material.

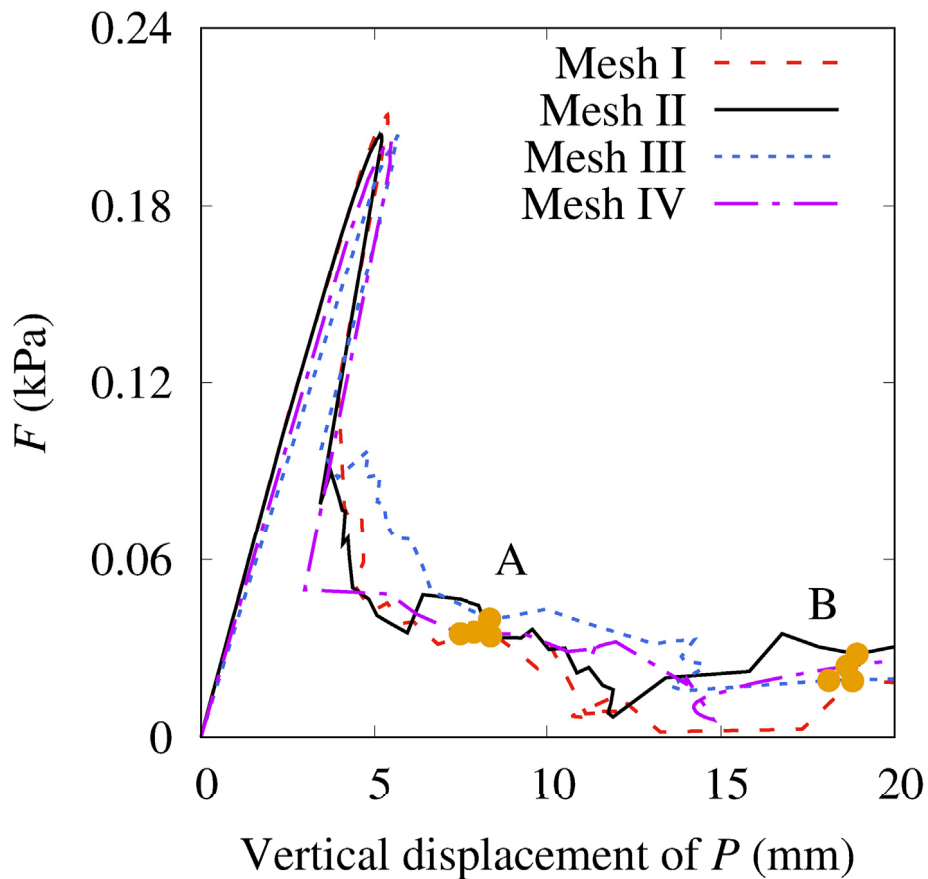


Fig. 18. Specimen with multiple cracks: force-displacement curves.

The force-displacement curves are shown in Fig. 18, indicating similar shapes. The snap-back parts are captured by the proposed method.

The crack paths at stage B are shown in Fig. 19, indicating similar cracking patterns. Crack opening and deformation plots are shown

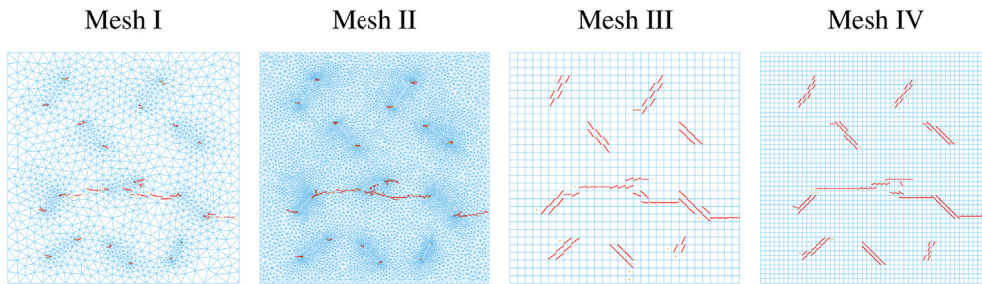


Fig. 19. Specimen with multiple cracks: crack paths at stage B.

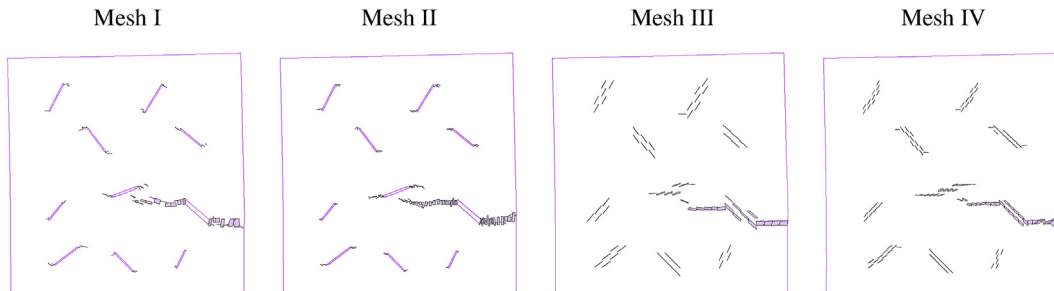


Fig. 20. Specimen with multiple cracks: crack opening plots ($\zeta_{eq} \geq \zeta_0$) with deformed boundaries (scale = 1:4) at stage A.

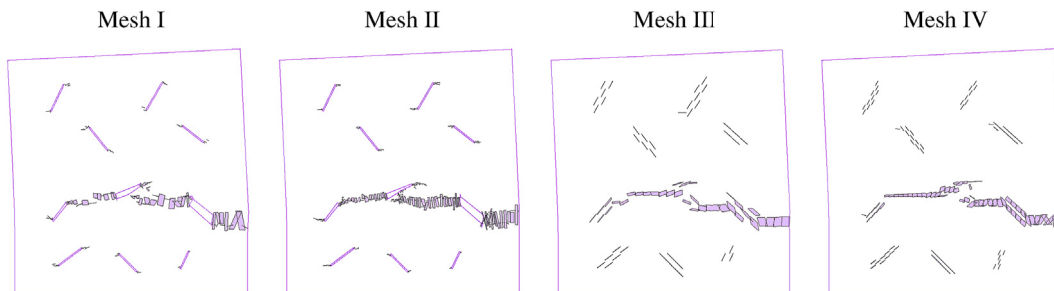


Fig. 21. Specimen with multiple cracks: crack opening plots ($\zeta_{eq} \geq \zeta_0$) with deformed boundaries (scale = 1:4) at stage B.

in Figs. 20 and 21. The results agree with the ones reported in Refs. [49,51]. The figures show similar results for different discretizations.

5. Conclusions

In this article, a direct dissipation-based arc-length approach was proposed in order to capture and trace the damage process of structures made of quasi-brittle materials in a stable and robust manner. In contrast to the internal energy and work done by the external loads, the dissipated energy was used directly in the proposed approach. It served as a monotonically increasing state variable. Moreover, when combined with the Sherman-Morrison formula, the stiffness factor of the arc-length constraint was obtained automatically. The approach was implemented in the framework of the CEM. Its effectiveness and reliability were demonstrated by several benchmark tests. The force-displacement curves were continuously traced.

Novelty

Main novelties of our work are:

1. The proposed arc-length approach extracts the dissipated energy based on crack openings and tractions but not use internal energy and the work done by the external loads.
2. The stiffness factor of the arc-length restraint is obtained by means of the Sherman-Morrison formula.

3. The proposed arc-length approach is built in the framework of the Cracking Elements Method (CEM).

Declaration of competing interest

The authors declared that they have no conflict of interest to this work.

Acknowledgements

The authors gratefully acknowledge financial support by the National Natural Science Foundation of China (NSFC) (51809069) and by the Hebei Province Natural Science Fund E2019202441.

References

- [1] Q.S. Nguyen, Bifurcation and Stability of Time-independent Standard Dissipative Systems, vol. 327, Springer, Vienna, 1993, pp. 45–94.
- [2] S. May, J. Vignollet, R. de Borst, A new arc-length control method based on the rates of the internal and the dissipated energy, Eng. Comput. 33 (1) (2016) 100–115.
- [3] R. de Borst, Computation of post-bifurcation and post-failure behavior of strain-softening solids, Comput. Struct. 25 (2) (1987) 211–224.
- [4] M.A. Gutiérrez, Energy release control for numerical simulations of failure in quasi-brittle solids, Commun. Numer. Methods Eng. 20 (1) (2004) 19–29.
- [5] C.V. Verhoosel, J.J.C. Remmers, M.A. Gutiérrez, A dissipation-based arc-length method for robust simulation of brittle and ductile failure, Int. J. Numer. Methods Eng. 77 (9) (2008) 1290–1321.

- [6] N. Singh, C. Verhoosel, R. de Borst, E. van Brummelen, A fracture-controlled path-following technique for phase-field modeling of brittle fracture, *Finite Elem. Anal. Des.* 113 (2016) 14–29.
- [7] İ. Özdemir, An alternative implementation of the incremental energy/dissipation based arc-length control method, *Theor. Appl. Fract. Mech.* 100 (2019) 208–214.
- [8] N.A. Labanda, S.M. Giusti, B.M. Luccioni, A path-following technique implemented in a Lagrangian formulation to model quasi-brittle fracture, *Eng. Fract. Mech.* 194 (2018) 319–336.
- [9] Y. Wang, H. Waisman, Progressive delamination analysis of composite materials using XFEM and a discrete damage zone model, *Comput. Mech.* 55 (1) (2015) 1–26.
- [10] E.C. Mejia Sanchez, L.F. Paullo Muñoz, D. Roehl, Discrete fracture propagation analysis using a robust combined continuation method, *Int. J. Solid Struct.* 193–194 (2020) 405–417.
- [11] Y. Zhang, X. Zhuang, Cracking elements: a self-propagating strong discontinuity embedded approach for quasi-brittle fracture, *Finite Elem. Anal. Des.* 144 (2018) 84–100.
- [12] Y. Zhang, X. Zhuang, Cracking elements method for dynamic brittle fracture, *Theor. Appl. Fract. Mech.* 102 (2019) 1–9.
- [13] T. Rabczuk, G. Zi, S. Bordas, H. Nguyen-Xuan, A simple and robust three-dimensional cracking-particle method without enrichment, *Comput. Methods Appl. Mech. Eng.* 199 (2010) 2437–2455.
- [14] T. Rabczuk, T. Belytschko, Cracking particles: a simplified meshfree method for arbitrary evolving cracks, *Int. J. Numer. Methods Eng.* 61 (2004) 2316–2343.
- [15] T. Rabczuk, T. Belytschko, A three-dimensional large deformation meshfree method for arbitrary evolving cracks, *Comput. Methods Appl. Mech. Eng.* 196 (2007) 2777–2799.
- [16] S. Saloustros, M. Cervera, L. Pelà, Challenges, tools and applications of tracking algorithms in the numerical modelling of cracks in concrete and masonry structures, *Arch. Comput. Methods Eng.* 26 (2019) 961–1005.
- [17] Y. Zhang, Z. Gao, Y. Li, X. Zhuang, On the crack opening and energy dissipation in a continuum based disconnected crack model, *Finite Elem. Anal. Des.* 170 (2020), <https://doi.org/10.1016/j.finel.2019.103333>.
- [18] M. Cervera, J.-Y. Wu, On the conformity of strong, regularized, embedded and smeared discontinuity approaches for the modeling of localized failure in solids, *Int. J. Solid Struct.* 71 (2015) 19–38.
- [19] Y. Zhang, H.A. Mang, Global cracking elements: a novel tool for Galerkin-based approaches simulating quasi-brittle fracture, *Int. J. Numer. Methods Eng.* 121 (2020) 2462–2480.
- [20] C. Geuzaine, J.-F. Remacle, Gmsh: A 3-d finite element mesh generator with built-in pre- and post-processing facilities, *Int. J. Numer. Methods Eng.* 79 (11) (2009) 1309–1331.
- [21] Y. Zhang, R. Lackner, M. Zeiml, H. Mang, Strong discontinuity embedded approach with standard SOS formulation: element formulation, energy-based crack-tracking strategy, and validations, *Comput. Methods Appl. Mech. Eng.* 287 (2015) 335–366.
- [22] G. Meschke, P. Dumstorff, Energy-based modeling of cohesive and cohesionless cracks via X-FEM, *Comput. Methods Appl. Mech. Eng.* 196 (2007) 2338–2357.
- [23] Y. Zhang, X. Zhuang, A softening-healing law for self-healing quasi-brittle materials: analyzing with strong discontinuity embedded approach, *Eng. Fract. Mech.* 192 (2018) 290–306.
- [24] X. Su, Z. Yang, G. Liu, Monte Carlo simulation of complex cohesive fracture in random heterogeneous quasi-brittle materials: a 3d study, *Int. J. Solid Struct.* 47 (17) (2010) 2336–2345.
- [25] J. Simo, F. Armero, Geometrically non-linear enhanced strain mixed methods and the method of incompatible modes, *Int. J. Numer. Methods Eng.* 33 (1992) 1413–1449.
- [26] J. Mosler, G. Meschke, 3D modelling of strong discontinuities in elastoplastic solids: fixed and rotating localization formulations, *Int. J. Numer. Methods Eng.* 57 (2003) 1553–1576.
- [27] J. Oliver, A. Huespe, E. Samaniego, A study on finite elements for capturing strong discontinuities, *Int. J. Numer. Methods Eng.* 56 (2003) 2135–2161.
- [28] R.I. Borja, Assumed enhanced strain and the extended finite element methods: a unification of concepts, *Comput. Methods Appl. Mech. Eng.* 197 (2008) 2789–2803.
- [29] J. Oliver, A consistent characteristic length for smeared cracking models, *Int. J. Numer. Methods Eng.* 28 (1989) 461–474.
- [30] M. Cervera, M. Chiumenti, Smeared crack approach: back to the original track, *Int. J. Numer. Anal. Methods GeoMech.* 30 (2006) 1173–1199.
- [31] L. Mu, Y. Zhang, Cracking elements method with 6-node triangular element, *Finite Elem. Anal. Des.* 177 (2020) 103421.
- [32] P. Helnwein, Some remarks on the compressed matrix representation of symmetric second-order and fourth-order tensors, *Comput. Methods Appl. Mech. Eng.* 190 (2001) 2753–2770.
- [33] Y. Zhang, Research Webpage with Fortran Subroutines Used in the Cracking Elements Method, 2021, <https://www.researchgate.net/profile/Yiming-Zhang-34/research>.
- [34] J.-Y. Wu, F.-B. Li, S.-L. Xu, Extended embedded finite elements with continuous displacement jumps for the modeling of localized failure in solids, *Comput. Methods Appl. Mech. Eng.* 285 (2015) 346–378.
- [35] M. Xie, W. Gerstle, Energy-based cohesive crack propagation modeling, *J. Eng. Mech.* 121 (1995) 1349–1358.
- [36] P. Dumstorff, G. Meschke, Crack propagation criteria in the framework of X-FEM-based structural analyses, *Int. J. Numer. Anal. Methods GeoMech.* 31 (2007) 239–259.
- [37] PARDISO solver project. <https://www.pardiso-project.org>.
- [38] D. Kourounis, A. Fuchs, O. Schenk, Toward the next generation of multiperiod optimal power flow solvers, *IEEE Trans. Power Syst.* 33 (2018) 4005–4014.
- [39] MUMPS: MULTifrontal massively parallel sparse direct solver. <http://mumps.enseiht.fr/>.
- [40] P. Amestoy, I. Duff, J.-Y. L'Excellent, Multifrontal parallel distributed symmetric and unsymmetric solvers, *Comput. Methods Appl. Mech. Eng.* 184 (2000) 501–520.
- [41] P.R. Amestoy, I.S. Duff, J.-Y. L'Excellent, X.S. Li, Impact of the implementation of MPI point-to-point communications on the performance of two general sparse solvers, *Parallel Comput.* 29 (2003) 833–849.
- [42] P. Bocca, A. Carpinteri, S. Valente, Mixed mode fracture of concrete, *Int. J. Solid Struct.* 27 (1991) 1139–1153.
- [43] J. Oliver, A. Huespe, M. Pulido, E. Chaves, From continuum mechanics to fracture mechanics: the strong discontinuity approach, *Eng. Fract. Mech.* 69 (2002) 113–136.
- [44] M. Geers, R.D. Borst, R. Peerlings, Damage and crack modeling in single-edge and double-edge notched concrete beams, *Eng. Fract. Mech.* 65 (2000) 247–261.
- [45] T.C. Gasser, G.A. Holzapfel, Modeling 3D crack propagation in unreinforced concrete using PUFEM, *Comput. Methods Appl. Mech. Eng.* 194 (2005) 2859–2896.
- [46] Z. Yang, J. Chen, Fully automatic modelling of cohesive discrete crack propagation in concrete beams using local arc-length methods, *Int. J. Solid Struct.* 41 (2004) 801–826.
- [47] P. Areias, D. Dias-da Costa, J. Alfaiate, E. Júlio, Arbitrary bi-dimensional finite strain cohesive crack propagation, *Comput. Mech.* 45 (Dec 2009) 61–75.
- [48] E. Lorentz, P. Badel, A new path-following constraint for strain-softening finite element simulations, *Int. J. Numer. Methods Eng.* 60 (2) (2004) 499–526.
- [49] E. Budyn, G. Zi, N. Moës, T. Belytschko, A method for multiple crack growth in brittle materials without remeshing, *Int. J. Numer. Methods Eng.* 61 (10) (2004) 1741–1770.
- [50] G. Zi, J.-H. Song, E. Budyn, S.-H. Lee, T. Belytschko, A method for growing multiple cracks without remeshing and its application to fatigue crack growth, *Model. Simulat. Mater. Sci. Eng.* 12 (jul 2004) 901–915.
- [51] T. Rabczuk, H. Ren, A peridynamics formulation for quasi-static fracture and contact in rock, *Eng. Geol.* 225 (2017) 42–48.